Research Article GU J Sci, Part A, 12(3): 873-893 (2025) 10.54287/gujsa.1737897

Gazi University
Journal of Science
PART A: ENGINEERING AND INNOVATION
http://dergipark.org.tr/gujsa

A Compact Multimodal Patch for Continuous and Electrode-Free Cardiopulmonary Monitoring

Beren SEMİZ[1*]

[1] Koc University, Department of Electrical and Electronics Engineering, Istanbul, Türkiye

Keywords

Wearable Devices
Health Monitoring
Seismocardiogram
Photoplethysmogram
Biomedical Signal Processing
Temperature Sensing

Abstract

Continuous and non-invasive cardiopulmonary monitoring is essential for the early detection and management of both chronic and acute health conditions. This study presents a compact, multimodal wearable patch that captures seismocardiogram (SCG), dual-wavelength photoplethysmogram (PPG), and skin temperature signals without requiring gel electrodes or form factor-limited designs. The system integrates low-noise sensors and a custom-designed PCB within a 3D-printed enclosure, resulting in a lightweight, electrode-free device suitable for a wide range of users. Experimental validation with 12 participants demonstrated accurate estimation of heart rate (HR), heart rate variability (HRV), respiratory rate (RR), and temperature, with low mean percentage errors across all modalities. HR and HRV were estimated with errors below 1%, RR with a mean error of 1.6%, and temperature within a 3.7% error margin. Additionally, the application of Teager-Kaiser energy operator improved the robustness of peak detection in SCG signals, leading to more accurate and reliable HR and HRV estimation. Unlike many existing wearables that rely on adhesive electrodes or single-signal modalities, this system offers a miniaturized, multi-sensor solution for continuous cardiopulmonary monitoring, suitable for both clinical environments and daily-life integration.

Cite

Semiz, B. (2025). A Compact Multimodal Patch for Continuous and Electrode-Free Cardiopulmonary Monitoring. *GU J Sci, Part A*, *12*(3), 873-893. doi:10.54287/gujsa.1737897

Author ID (ORCID Number)

0000-0002-7544-5974 Beren SEMİZ

Article Process

Submission Date 08.07.2025
Revision Date 22.07.2025
Accepted Date 15.08.2025
Published Date 30.09.2025

1. INTRODUCTION

Cardiovascular and cardiopulmonary diseases are among the most prevalent and life-threatening health conditions worldwide according to the World Health Organization (WHO, 2024). Based on the recent statistics, the top five causes of death are ischaemic heart disease (9.1 million deaths, ~13%), COVID-19 (8.8 million, ~12.5%), stroke (6.5 million, ~9.3%), chronic obstructive pulmonary disease (3.3 million, ~4.7%), and lower respiratory infections (2.5 million, ~3.5%). Many of these conditions, particularly chronic diseases, progress silently over time and may go undetected without continuous physiological monitoring. Thus, the ability to capture real-time, long-term data is essential for proactive healthcare delivery, timely clinical interventions and personalized treatment scheduling (Sana et al., 2020).

*Corresponding Author, e-mail: corresponding@author.com

This work is licensed under Creative Commons Attribution-ShareAlike 4.0 International.

In medical settings, diagnosis and patient follow-up primarily rely on assessing vital parameters such as heart rhythm, blood pressure, body temperature, and respiratory rate, along with heart, lung, and vascular assessments. Therefore, there is a growing demand for innovative wearable technologies that can digitize these conventional examination practices and enable continuous, clinically reliable health monitoring beyond hospital environments (Gupta et al., 2025). Recent advances in wearable sensors, microelectronics and biomedical signal processing have enabled the development of lightweight, battery-powered systems capable of measuring a variety of physiological signals noninvasively. These systems are particularly valuable for monitoring vital signs such as heart rate (HR), respiration rate (RR), and skin temperature, regardless of time and place.

Among physiological signals, seismocardiogram (SCG) and photoplethysmogram (PPG) have gained significant attention due to their ability to characterize cardiovascular and respiratory function without the need for adhesive electrodes or direct access to electrical cardiac signals such as the electrocardiogram (ECG). SCG captures the mechanical vibrations on the chest wall caused by myocardial contractions and valve movements, offering insights into cardiac mechanics such as the aortic opening (AO) and mitral valve closure (MC) (Inan et al., 2014). Studies have demonstrated that the SCG signal can provide clinically valuable information without the need for invasive methods, such as systolic time interval estimation (Shandhi et al., 2019), valvular heart disease, atrial fibrillation or aortic stenosis evaluation (Hurnanen et al., 2016; Yang et al., 2019; Erin & Semiz, 2023), heart failure classification (Inan et al., 2018), and hemodynamic parameter estimation like stroke volume (Semiz et al., 2020). On the other hand, PPG measures pulsatile blood volume changes in the microvasculature, typically using light emitted and detected through skin tissues, and provides information on blood oxygenation, pulse timing, and vascular health (cheol Jeong et al., 2018; Nwibor et al., 2023; Chen et al., 2024).

Several prototypes have focused on individual physiological signals such as ECG, SCG, or PPG for heart rate and rhythm assessment (Fattah et al., 2017; Li et al., 2017; Loro et al., 2024; Gupta et al., 2025), yet only a limited number of systems have integrated these modalities for more comprehensive cardiovascular and cardiopulmonary monitoring. For example, Zavanelli et al. (2021) designed a soft patch capable of simultaneously recording ECG, PPG, and pulse vibrations, whereas Klum et al.'s (2020) 'wearable stethoscope' focused on ECG and phonocardiogram acquisition. While Etemadi et al. (2015) proposed a multimodal device for ECG, SCG, environmental temperature, and pressure monitoring; we have also developed a multi-modal system to acquire ECG, SCG, PPG and temperature signals (Hayirlioglu & Semiz, 2024). A detailed comparison of these systems is provided in Table 1. We validated our previous system both in laboratory settings with healthy volunteers and in clinical environments with pediatric patients (Hayirlioglu & Semiz, 2024; Semiz, 2025). While the system demonstrated feasibility, several practical limitations became evident during testing. Most notably, the device's relatively large size (approximately 10 cm) made it unsuitable for users of different ages, body sizes, and anatomical characteristics. This bulkiness also

compromised the reliability of signals requiring direct skin contact, such as PPG and temperature. Moreover, the use of gel electrodes introduced concerns regarding ease of use and comfort, particularly in long-term applications. Battery life was another constraint, as it did not support extended monitoring sessions. These limitations highlighted the need for a more compact, user-friendly, and adaptable solution, which ultimately led to the development of the current system.

In this work, we present a compact, multimodal wearable patch that captures SCG, PPG (red and infrared), and body temperature signals for cardiopulmonary monitoring. The system features a custom-designed PCB with integrated sensors, microcontroller, and data storage. The hardware, comprising a modular layout, FFR cabling, and a 3D-printed low-profile case, was optimized for comfort and adaptability. The term *electrode-free* refers to the absence of traditional gel-based or dry-contact electrodes (as in ECG acquisition); instead, our system relies on SCG and PPG sensing for physiological measurements. The term *patch* describes the compact, wearable form factor (approximately 3.5 × 4 cm, ~21 g) that can be directly affixed to the body without wires or bulky accessories. This miniaturized design supports easy integration into daily life and makes the system suitable not only for adult users but also adaptable to pediatric, geriatric, and mobility-impaired populations. Such adaptability is critical for ensuring comfort across a broad range of use cases, from daily wellness tracking to clinical rehabilitation and home-based cardiopulmonary assessment.

Table 1. *Specifications of the related works*

Device	Signals & Parameters	Sampling Rates	Specifications
(Hayirlioglu & Semiz, 2024)	ECG, SCG, PPG, Temperature	500 Hz, 500 Hz, 200 Hz, 25 Hz	**Size:** 10 x 10 cm **Weight:** 23.6 g **Battery:** 3 hours (400 mAh LiPo)
(Etemadi et al., 2015)	ECG, SCG, Environmental Temperature and Pressure	500 Hz, 500 Hz, 10 Hz, 10 Hz	**Size:** 4.6 x 10.8 cm (+case) **Weight:** 38.2 g **Battery:** 50 hours (LIR2450)
(Gupta et al., 2020)	SCG	8 kHz	**Size:** Custom 2 x 2 cm sensor is positioned between two layers of 4-inch-wide (10.2 cm) elastic bands. **Weight:** Not Specified **Battery:** Not Specified
(Zavanelli et al., 2021)	SCG, ECG, PPG	500 Hz, 120 Hz, 200 Hz	**Size:** 3 x 3 cm (based on the figure) **Weight:** Not specified **Battery:** 10 hours (150 mAh LiPo)
(Klum et al., 2020)	ECG, Phonocardiogram	1 kHz, 10 khZ	**Size:** 7 x 6 cm **Weight:** Not specified **Battery:** 10 hours (450 mAh LiPo)

2. MATERIAL AND METHOD

2.1. Sensor Selection

In the literature, SCG signal analysis is generally performed at frequencies below 100 Hz, and a sampling rate of 500 Hz has been shown to be sufficient (Semiz et al., 2020). Although analog accelerometers offer a wider bandwidth than digital ones, the sensor selected for this project prioritizes characteristics such as low noise, high resolution, and sensitivity capable of capturing peak-to-peak amplitude variations within <10 mg, rather than high bandwidth. Therefore, the ADXL355 (Analog Devices, Norwood, MA, USA) accelerometer, which has a noise floor of 25 μg/√Hz and a resolution of 0.003 mV/bit and has been successfully used in prior studies was selected for the designed system (Ganti et al., 2020; Hayirlioglu & Semiz, 2024).

For the PPG sensor, existing systems were examined. Smartwatches commonly use green LEDs, which are less sensitive to motion-induced noise compared to infrared and red LEDs. However, due to their shorter wavelength, green LED-based PPG systems can only measure the microvascular network on the skin surface (Maeda et al., 2011; Lee et al., 2013). On the other hand, red and infrared LEDs can penetrate deeper tissues where arteries are located. Therefore, for the PPG system design, sensors that include red and infrared LEDs were preferred. The MAX30102 (Maxim Integrated, Sunnyvale, CA, USA) digital sensor, offering 0.05 mV/bit resolution and a sampling rate of 3200 samples per second, was found suitable for acquiring PPG signals. Since the selected sensor contains both red and infrared LEDs, it can potentially enable oxygen saturation measurement as well.

The MAX30102 and ADXL355 sensors both support I2C communication. While the MAX30102 supports a maximum SCL frequency of 400 kHz, the ADXL355 supports up to 3.4 MHz. Thus, if the same signal line is used, the I2C communication speed will be limited to a maximum of 400 kHz. Considering system requirements and the targeted sampling rate, this speed was deemed sufficient. The FIFO memory integrated into both the ADXL355 and MAX30102 allows for synchronized and consistent data collection.

For body temperature measurement, the MAX30205 (Analog Devices) digital sensor was selected. It operates between 0℃ and 50℃, provides 3.90625 mV/℃ resolution, ± 0.1℃ accuracy in the 37.0-39.0 ℃ range, and ± 0.2℃ accuracy in the 35.8-37.0 ℃ and 39.0-41.0 ℃ ranges. The signal is sampled at 25 Hz and digitally transmitted to the microcontroller via the I2C interface.

Microcontroller selection was based on the device's (i) ability to collect data at the desired speed, (ii) low power consumption, (iii) ample program memory, (iv) internal ADC, and (v) sufficient number of digital I/O pins. The Atmega328pb microcontroller was selected as it meets these requirements. It features 32 KBytes of memory, 1 KByte EEPROM, 23 programmable I/O lines, and an 8.000 MHz crystal oscillator. It consumes 3 mA current in active mode at 3.3V, and only 0.1 μA in deep sleep mode. It also includes one 16-bit timer and two hardware interrupts, making it a preferred choice.

Recorded data are written to an SD card. A 16GB SanDisk Ultra with a write speed of 80 MB/s was selected. For integration with the system, a Molex 5025700893 SMD connector is used. The naming of files written to the SD card is based on real-time timestamps obtained from the MCP7940n RTC module. The file name reflects the exact hour, minute, and second the recording started, making the start time of each recording clearly identifiable. The system is powered by a 400 mAh rechargeable lithium battery. The battery is safely charged without risk of overheating by the LTC4062 chip (Analog Devices), which features thermal regulation.

2.2. Firmware Design

To enable the system to communicate with sensors and record data, embedded software has also been developed. The block diagram of the system is presented in Figure 1. During development, in addition to open-source Arduino libraries, the following open-source libraries were used:

- SdFat, Author: Bill Greiman, Version: 2.1.2
- SparkFun MAX3010x Pulse and Proximity Sensor Library, Author: SparkFun Electronics, Version: 1.1.1
- MCP7940, Author: SV-Zanshin, Version: 1.2.0
- Max30205, Author: Protocentral, Version: 2.1.1

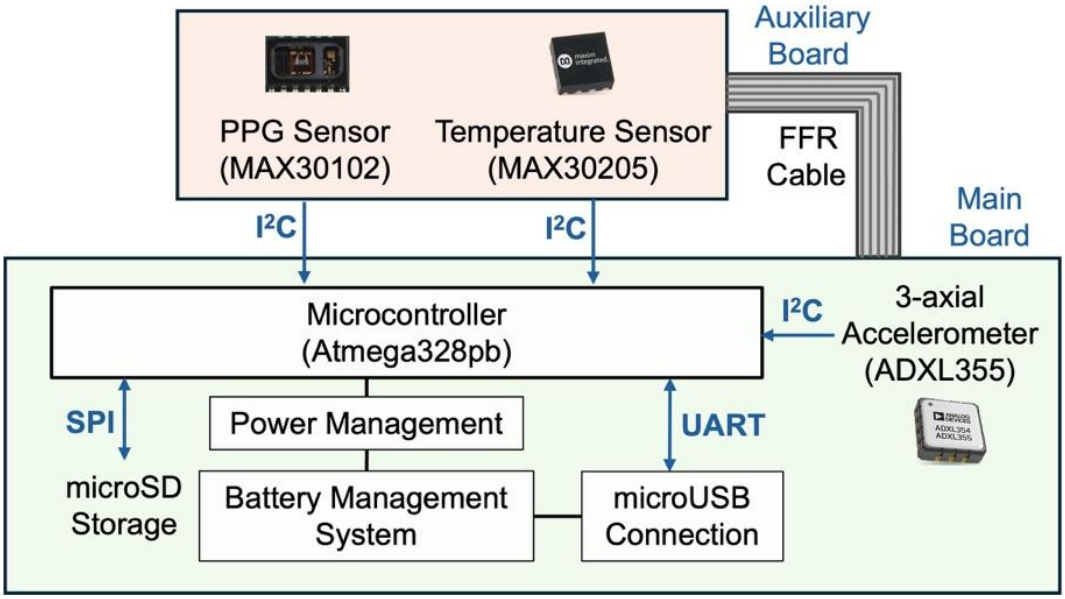


Figure 1. *Block diagram of the system*

The accelerometer, PPG, and temperature sensors are sampled at 500 Hz, 200 Hz, and 25 Hz, respectively. These sensors store data in their respective FIFOs at the specified sampling rates. The microcontroller reads the data from the FIFOs and temporarily stores it in its memory. Every 40 ms, the accumulated data is written in batches to the SD card. This batch-writing approach is preferred because it significantly reduces the time required for writing compared to writing each sample individually and ensures that data is always written in the same sequence. *Start* and *Stop* commands for data recording are controlled by two buttons accessible to the user. Since these buttons are connected to the hardware interrupts of the microcontroller, pressing the start

button initiates recording without delay, and pressing the stop button halts recording immediately, closing the file on the SD card automatically.

2.3. Printed Circuit Board (PCB) Design and Fabrication

The designed printed circuit boards (PCBs) are shown in Figure 2. The PCB consists of two separate boards: a 6-layer main board and a 2-layer auxiliary board that hosts the PPG and temperature sensors. The auxiliary board has been positioned to make direct contact with the skin and is directly connected to the main board. The connection between the two boards has been established using an FFR (flat flex ribbon) cable, allowing the overall thickness of the prototype to be minimized. Additional pins have been included in the design to accommodate a Bluetooth module if it is needed in the future. A large ground (GND) plane was created in the design to reduce the influence of potential noise sources in the circuit on the measurements. Instead of standard HASL, Electroless Nickel Immersion Gold (ENIG) was chosen. As the PCB substrate material, FR4-Standard TG 135–140 was used due to its low inductance and low dielectric constant. The main PCB has a size of 4 cm * 3.5 cm. After fabrication, the PCB was placed inside a 3D-printed case (Figure 3). The whole system was weighing approximately 21 grams. Considering that the 41 mm Apple Watch Series 9 weighs 31.5 g and the 45 mm version weighs 38.7 g, the proposed system does not pose any usability challenges for the user. With the current sampling rates, the maximum continuous recording duration is 7.5 hours. This produces a .txt file of approximately 200 MB in size.

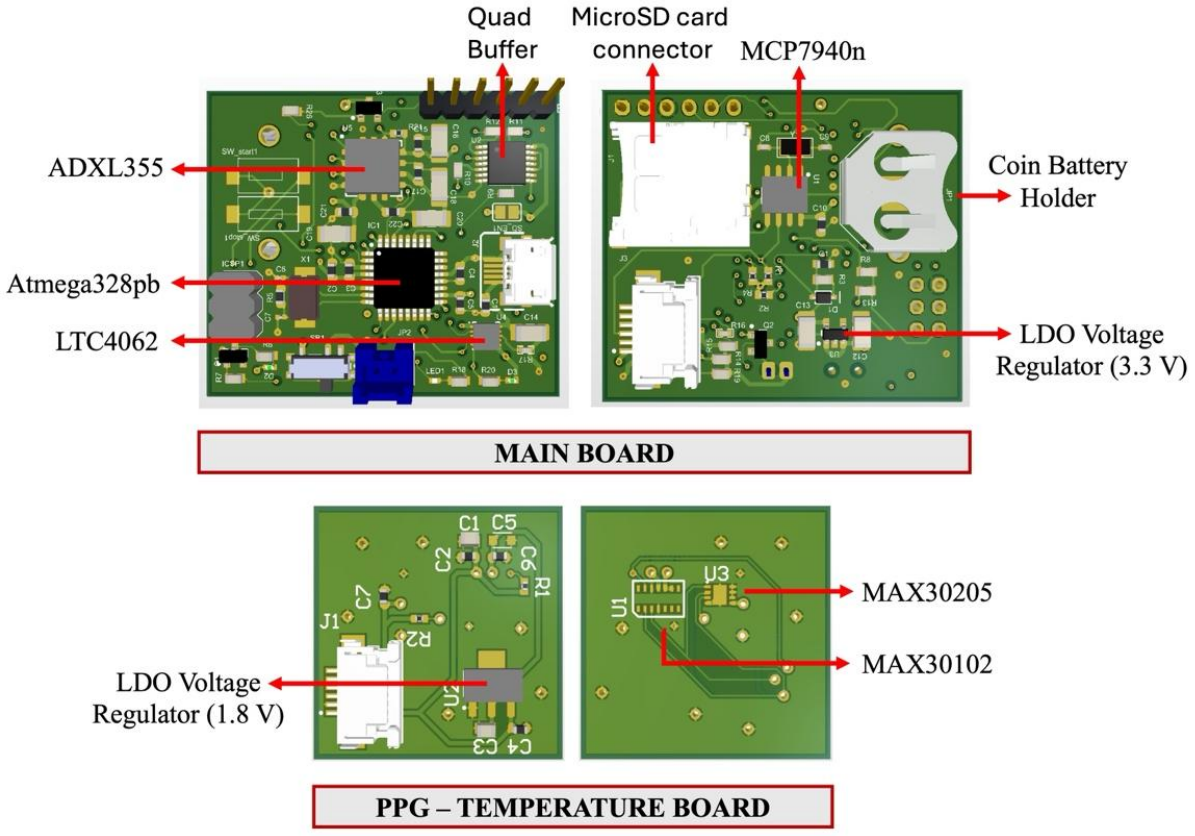


Figure 2. *The designed printed circuit boards*

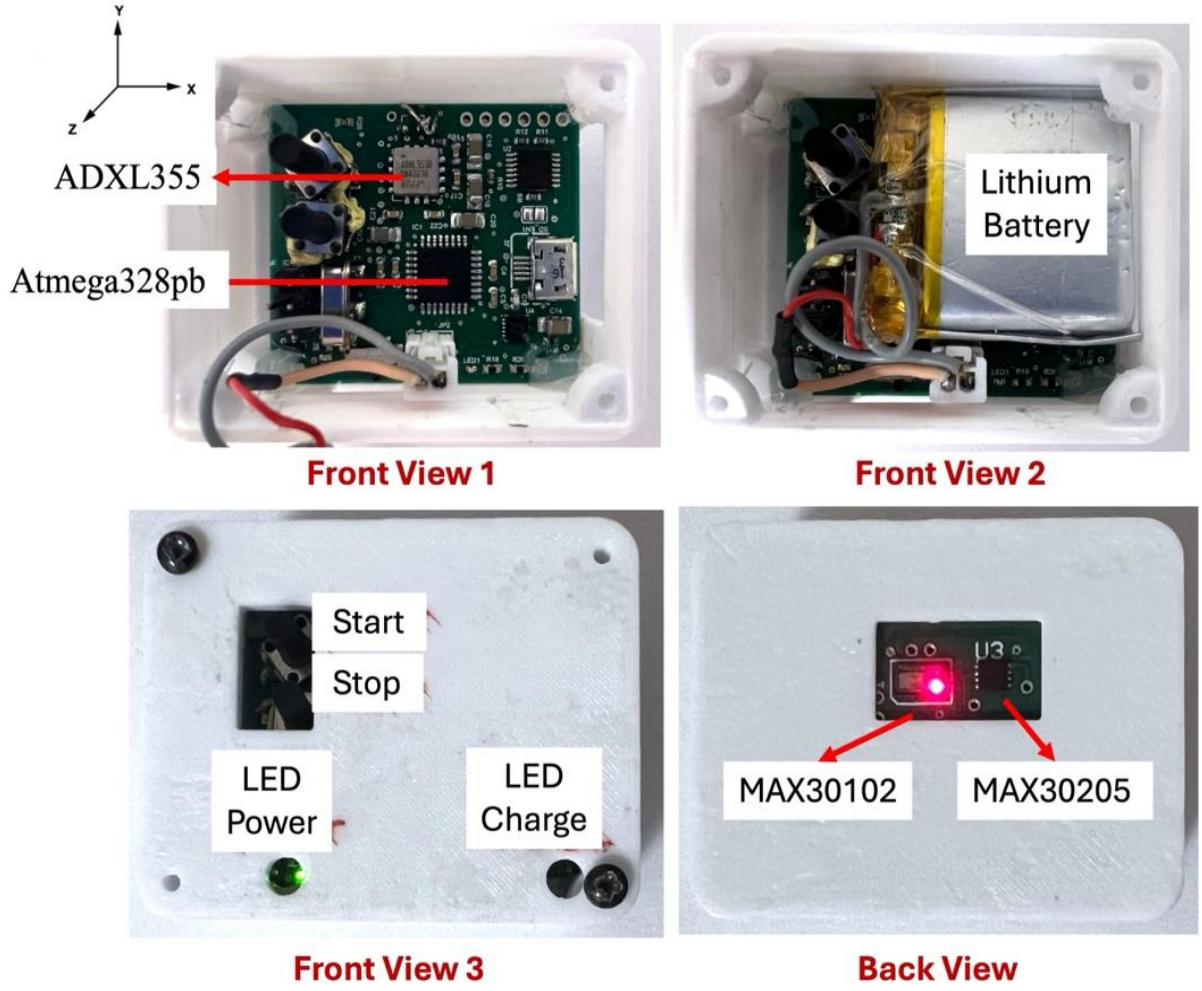


Figure 3. *The final design of the system (front and back)*

2.4. Data Collection for Validation Tests

This study was conducted under a protocol approved by the Koç University Institutional Review Board (2024.358.IRB2.155). Reference ECG and respiration data were recorded using the BIOPAC system. The RSPEC-R module of the BIOPAC system wirelessly transfers the ECG signal (measured via electrodes) and the abdominal expansion-contraction data (measured via a respiratory belt) to the BIOPAC system, allowing continuous acquisition of reference signals. The patch was placed on the mid-sternum vertically as shown in Figure 4. Thus, the X, Y, Z axes were corresponding to the head-to-foot, lateral and dorso-ventral directions, respectively. For patch mounting, Roll Trans Transparent Medical Tape was used, however the system can also be attached through a belt or embedded inside clothing.

Before starting the experimental protocol, participants' demographic information, including age, weight, sex, and height, was recorded. Following this, physiological parameters such as body temperature, oxygen saturation (SpO_2), heart rate (HR), and systolic and diastolic blood pressure (SBP and DBP) were measured. A Comfort non-contact infrared thermometer was used for temperature, a Comfort Plus fingertip pulse oximeter for oxygen saturation, and the Omron M2 device for heart rate and blood pressure. During data

collection, the participants were asked to stand still for five minutes. Throughout the entire experimental protocol, physiological signals from the patch were recorded onto an SD card, while reference signals were simultaneously collected using the BIOPAC system. The study included 12 participants (7 females, 5 males). Their demographic characteristics and the hemodynamic parameters are presented in Table 2.

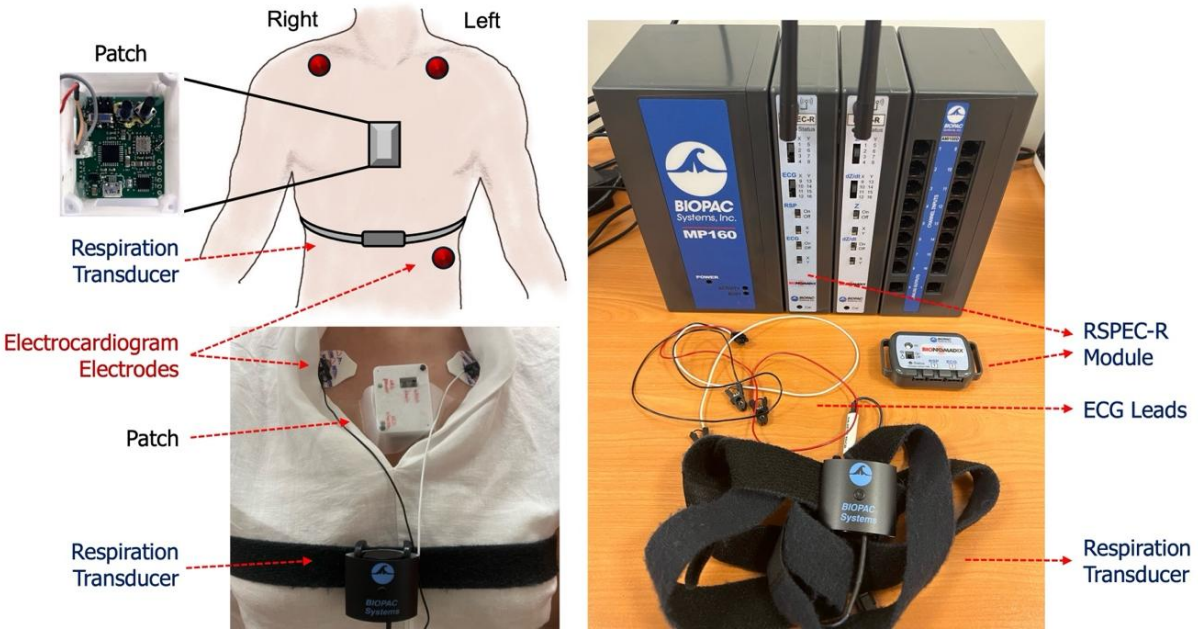


Figure 4. *Sensor placement*

Table 2. *Subject demographics and hemodynamic parameters*

ID	Age (years)	Height (cm)	Weight (kg)	Gender	SpO_2 (%)	SBP (mmHg)	DBP (mmHg)	Temp. (°C)
1	27	178	73	F	99	116	75	36.4
2	33	167	53	F	99	99	75	36.5
3	29	163	52	F	99	118	76	36.4
4	32	161	55	F	100	132	84	36.6
5	32	166	60	F	99	125	79	36.3
6	34	171	57	F	99	140	90	36.8
7	32	164	60	F	99	110	72	36.1
8	31	180	75	M	98	145	92	36.5
9	35	180	79	M	98	122	78	36.7
10	35	190	99	M	99	135	88	36.6
11	30	187	85	M	98	128	82	36.0
12	35	176	81	M	99	115	75	36.2
mean ± SD	**32.1 ± 2.5**	**173.6 ± 9.7**	**69.1 ± 15.1**	**7F, 5M**	**98.8 ± 0.6**	**123.8 ± 13.2**	**80.5 ± 6.6**	**36.4 ± 0.2**

2.5. Signal Pre-processing

Following data acquisition, signal processing pipelines were designed to estimate hemodynamic parameters. For the SCG analysis, dorso-ventral SCG was used in parallel with the previous studies in the literature (Taebi et al., 2019). To minimize noise while preserving signal quality, the signals were processed using custom Kaiser window FIR bandpass filters based on the reported frequency ranges (Pandia et al., 2013; Carek et al., 2017; Shandhi et al., 2019). Summary of the selected frequency ranges were as follows:

- SCG: 1–40 Hz for heart rate and heart rate variability computation.
- SCG: 0–1 Hz for respiration rate calculation.
- PPG (red and IR): 1–15 Hz for heart rate and heart rate variability computation.
- PPG (red and IR): 0–1 Hz for respiration rate calculation.

In our custom Kaiser window FIR band-pass filter, the parameters *(Fstop1, Fpass1, Fpass2, Fstop2, Fs)* define the filter's frequency characteristics, where *Fstop1* and *Fstop2* are the lower and upper stopband edge frequencies, *Fpass1* and *Fpass2* are the lower and upper passband edge frequencies, and *Fs* is the signal's sampling frequency. Fixed values are used for the passband ripple (*Dpass* = 0.05, ~0.43 dB) and stopband attenuation (*Dstop1* = *Dstop2* = 0.001, 60 dB). The *kaiserord* function is used to estimate the minimum filter order required to meet the given frequency and attenuation specifications. The transition widths are determined by the differences between *Fstop1* and *Fpass1* (lower transition) and between *Fpass2* and *Fstop2* (upper transition). The filter is gain-normalized. The same function was used for both low-pass and bandpass filtering by adjusting the frequency parameters accordingly.

To facilitate peak detection, Gaussian filtering was then applied to the SCG and PPG signals to suppress motion artifacts. This involved convolving the signals with a Gaussian window, which smooths high-frequency noise while preserving essential signal features.

2.6. Derivation of Hemodynamic Parameters

2.6.1. Heart Rate and Heart Rate Variability Computation from SCG and PPG Signals

Reference heart rate (HR) and heart rate variability (HRV) values were calculated using the reference electrocardiogram (ECG) signal recorded by the BIOPAC system. First, max-min normalization was applied on the filtered signals. R-peaks were then identified on the waveform, and the intervals between successive R-peaks were computed to construct the RR interval vector. This vector was then used in Equations (1) and (2) to derive HR in beats per minute (bpm) and HRV in milliseconds (ms). For the BIOPAC-based computations, Fs value was 2 kHz.

$$HR = \frac{60 * Fs}{mean(RR)} \tag{1}$$

$$HRV = \sqrt{\frac{1}{N-1}\sum_{i=1}^{N-1}(RR_{i+1} - RR_i)^2} * \frac{1000}{Fs} \quad (2)$$

For the PPG signal, a similar pipeline was employed for HR and HRV computation. First, the peaks were detected on the Gaussian-windowed red and infra-red signals and the time intervals between consecutive peaks were calculated. This resulted in a PP vector similar to the RR vector we had in the ECG case. The HR and HRV were then computed using Equations 1 and 2, respectively. For the PPG-based computations, Fs value was 200 Hz.

On the other hand, for the SCG-based HR and HRV computation, a two-step pipeline was applied. First, a Teager Energy-based peak detection algorithm was implemented. The Teager energy operator, originally based on the energy of an oscillator, is effective at identifying rapid changes in signals - such as amplitude fluctuations, frequency shifts or abrupt transitions (Kaiser, 1990). In the context of SCG signals, accurately identifying aortic opening (AO) points using basic peak detection methods is challenging due to: (i) the presence of nearby peaks corresponding to mitral valve closure (MC) and aortic valve closure (AC), and (ii) noise introduced by motion artifacts and intrinsic signal variability, which can obscure AO events. Therefore, we hypothesized that the Teager energy operator could enhance the detection SCG AO peaks, especially in cases where conventional peak detection methods are not sufficient.

The Teager energy operator was selected for its unique ability to emphasize localized energy variations in physiological signals with minimal computational overhead. Unlike multiscale or adaptive methods such as Wavelet Transform (WT) or Empirical Mode Decomposition (EMD), which require tunable parameters and often suffer from mode mixing or edge effects, the Teager operator is a time-domain technique that captures instantaneous energy by leveraging both amplitude and frequency modulations. It is also non-iterative and parameter-free, making it suitable for real-time implementation on wearable or resource-constrained systems. However, the Teager operator is sensitive to high-frequency noise and may amplify minor fluctuations if proper pre-filtering is not applied. In contrast, WT or EMD offer better multiscale decomposition and denoising capabilities, but at the cost of higher computational load and increased complexity. Given our focus on simplicity, interpretability, and low-power applicability in wearable settings, the Teager Operator was deemed the most appropriate choice.

For any discrete-time signal, the Teager energy (Ψ) at a given time point is computed using three consecutive signal samples, as shown in Equation 3. In our implementation, the dorso-ventral SCG signal was first band-pass filtered (1-40 Hz) to suppress baseline drift and high-frequency noise. The Teager energy was calculated for the filtered SCG signal, and the upper envelope of the resulting energy signal was extracted to emphasize significant points corresponding to the aortic opening (AO) events. The envelope function was identifying local maxima and minima in the signal and using spline interpolation between these points to compute the

upper and lower envelopes. Negative envelope values were set to zero to avoid erroneous detections. The minimum allowable distance between consecutive peaks was set to half the SCG sampling rate, corresponding to 0.5 s at the given sampling frequency. The time intervals between detected AO points were then measured, and their average was used to estimate HR and HRV, as described in Equations 1 and 2. For the SCG-based computations, the sampling frequency was 500 Hz. The method has very few tunable parameters (mainly the envelope window length and minimum inter-peak distance), and no iterative optimization, making it computationally lightweight and suitable for real-time wearable applications.

For all HR and HRV derivations, the percent errors were computed using Equation 4; where *actual* is the reference ECG-based HR and HRV, and *calculated* is the PPG- and SCG-derived HR and HRV values.

$$\Psi_{TE}[\mathrm{n}] = x[n]^2 - \mathrm{x}[\mathrm{n}+1]\mathrm{x}[\mathrm{n}-1] \tag{3}$$

$$\%\, error = \frac{actual - calculated}{actual} * 100 \tag{4}$$

2.6.2. Respiration Rate Computation

To estimate respiration rate, two separate methods were applied: one based on the dorso-ventral SCG signal and the other on the PPG-Red signal. The red channel of the PPG was preferred over the infrared (IR) channel due to its relatively lower wavelength, which makes it less susceptible to motion artifacts. As described earlier, both signals were bandpass filtered between 0-1 Hz and smoothed using a Gaussian window. Peak-to-peak intervals were then extracted, with each peak-valley transition representing one exhalation-inhalation cycle. The resulting vector of peak-to-peak durations was used in a formula analogous to Equation 1 to compute the respiration rate in breaths per minute. Error values were again computed using Equation 4, where *actual* is the reference belt-derived RR and *calculated* is the PPG- and SCG-derived RR values.

2.6.3. Statistical Analyses

The agreement between the reference measurements and estimates obtained from SCG, PPG-red, PPG-IR, and temperature sensing was assessed using correlation and statistical difference tests. Pearson's correlation coefficient (r) was calculated to evaluate the strength of the linear relationship, while Spearman's rank correlation coefficient (ρ) was used to assess monotonic relationships without assuming normality. To detect systematic bias, the normality of paired differences (reference - estimate) was first assessed using the Shapiro-Wilk test. If normally distributed, a paired *t*-test was applied; otherwise, the Wilcoxon signed-rank test was used. Bland-Altman analysis was performed to quantify agreement by computing the mean bias, standard deviation (SD) of the differences, and 95% limits of agreement (LoA = bias ± 1.96 × SD). Additionally, the mean absolute error (MAE) was also reported along with the abovementioned percentage errors as a measure of average magnitude of error.

3. RESULTS AND DISCUSSION

3.1. Signal Quality

The signal quality in our recordings was sufficient across all sensor modalities, as shown in Figure 5. The figure illustrates the filtered (1-40 Hz) SCG signals (head-to-foot, lateral, and dorso-ventral), which exhibit clearly distinguishable cardiac-induced vibrations with minimal noise and motion artifacts. The figure also presents the red and infrared PPG signals, filtered (1-15 Hz) and processed with a Gaussian window, yielding clean, periodic waveforms with well-defined peaks that indicate reliable pulse detection. The sixth subplot shows the sample-averaged temperature measurement, which falls within acceptable ranges. As the last two subplots, the reference ECG and respiration measurements are presented.

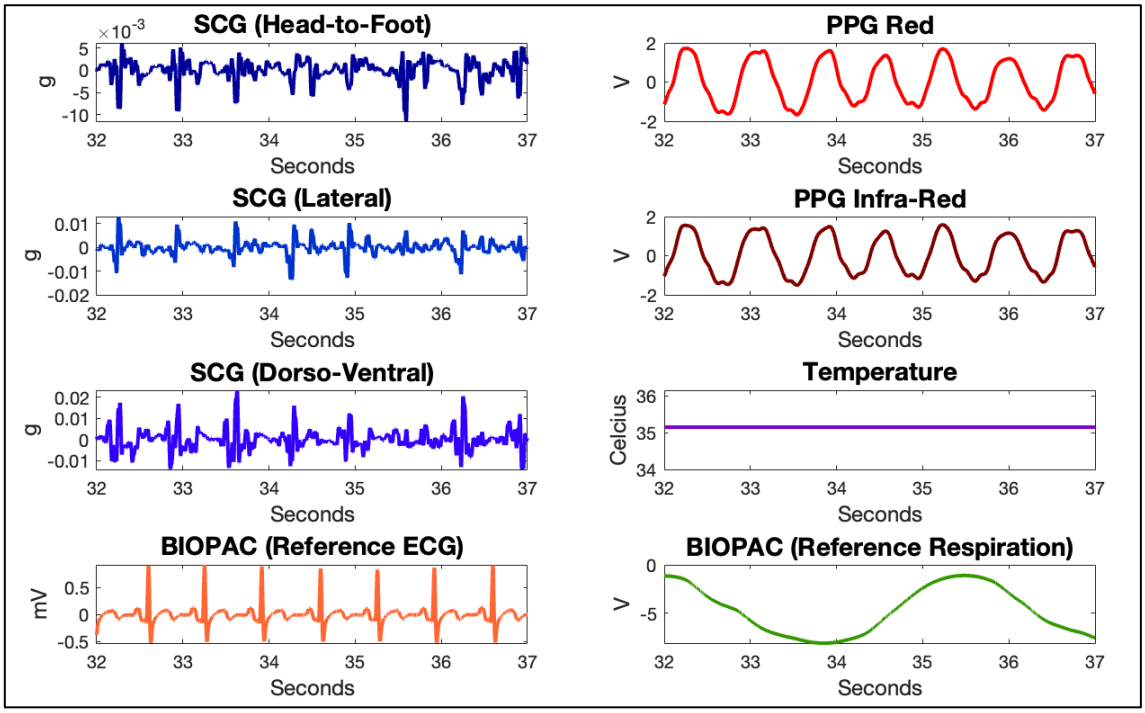


Figure 5. *Five-second-long pre-processed signal segments*

3.2. Heart Rate and Heart Rate Variability Computation Results

Figure 6 illustrates the impact of Teager-Kaiser energy operator in SCG processing. The top panel shows the filtered (1-40 Hz) dorso-ventral SCG signal, where cardiac-induced vibrations are present but not easily distinguishable in some cases, such as the region in green box. In contrast, the lower panel displays the corresponding Teager-Kaiser energy plot, where the signal has been transformed to highlight its instantaneous energy content. This transformation significantly enhances the visibility of cardiac peaks, enabling more robust and accurate peak detection. Red inverted triangles mark the detected peaks, which exhibit a regular rhythm aligned with the expected heartbeats. The green box highlights the specific region where the peaks have been particularly enhanced for peak detection. Hence, the use of the Teager-Kaiser Energy Operator proves to be a highly effective preprocessing technique for SCG, as it amplifies transient energy events in the signal, thereby improving signal-to-noise ratio and peak prominence.

Table 3 and 4 summarize the mean percentage error and standard deviation for HR and HRV measurements derived from PPG red, PPG IR, and SCG signals. SCG yielded the lowest mean errors for both HR ($0.6 \pm 0.4\%$) and HRV ($0.4 \pm 0.5\%$), outperforming both PPG red ($1.6 \pm 1.3\%$ for HR, $2.1 \pm 1.2\%$ for HRV) and PPG IR ($2.1 \pm 1.2\%$ for HR, $2.6 \pm 2.1\%$ for HRV). This indicates that SCG, when properly processed, can serve as a more reliable modality for cardiac monitoring compared to PPG, which is known to be more susceptible to motion artifacts and signal quality degradation under suboptimal conditions, such as chest-based measurements.

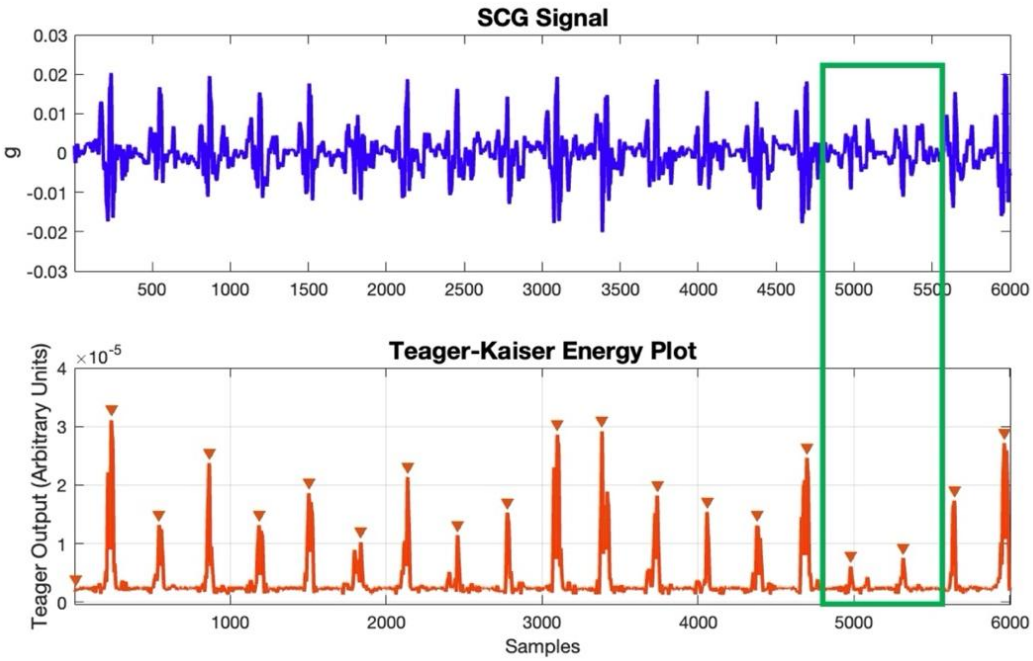


Figure 6. *Effect of Teager-Kaiser operator in peak enhancement*

The performance of the proposed approach was also benchmarked against commonly used methods in the literature, including direct peak detection, template matching with correlation analysis (Centracchio et al., 2023), empirical mode decomposition (Barnova et al., 2020), and wavelet decomposition (Lin & Jhou, 2020). Wavelet-based estimation resulted in error rates of $2.0 \pm 2.8\%$ for HR and 4.3 ± 6.6 % for HRV; empirical mode decomposition in error rates of $1.3 \pm 1.1\%$ for HR and 4.6 ± 7.2 % for HRV; and template-matching in error rates of $2.5 \pm 2.7\%$ for HR and $4.2 \pm 5.4\%$ for HRV. A high SD in the error values indicates large variability in performance across measurements or subjects, meaning that while some estimates may be accurate, others deviate substantially from the reference.

We then re-evaluated the SCG-based HR and HRV estimations without applying the Teager-Kaiser Operator, i.e., by directly performing peak detection on the filtered signal. We observed that when Teager-Kaiser Operator was not used, the percentage errors increased to $1.6 \pm 1.0\%$ for HR and $0.7 \pm 0.8\%$ for HRV. In contrast, when Teager-Kaiser Operator was applied, the errors were $0.6 \pm 0.4\%$ for HR and $0.4 \pm 0.5\%$ for HRV, as previously reported. To statistically assess the significance of this improvement, we performed a paired Wilcoxon signed-rank test. This non-parametric test was chosen because (i) the error distributions did

not meet normality assumptions, and (ii) the measurements were paired, as both conditions were derived from the same subjects. The results showed that the reduction in HR error was statistically significant ($p = 0.0049$), whereas the difference in HRV error was not ($p = 0.57$), considering an alpha value of 0.05. Given the inherently higher variability in HRV, this outcome was indeed expected. These findings demonstrate that Teager-Kaiser Operator contributes to more accurate and reliable HR and HRV estimation from SCG.

Table 3. *Heart rate (HR) values in beats per minute (bpm) and % errors*

ID	Reference HR	PPG Red HR	PPG I HR	SCG HR	PPG Red HR % error	PPG IR HR % error	SCG HR % error
1	92.7	95.6	91.2	93.5	3.1	1.6	0.9
2	82.6	81.6	83.3	82.9	1.2	0.8	0.4
3	86.7	86.8	83.8	86.2	0.1	3.3	0.6
4	84.2	82.8	81.4	84.7	1.7	3.3	0.6
5	82.6	85.6	84.3	83.8	3.6	2.1	1.5
6	64.9	64.3	66.8	64.3	0.9	2.9	0.9
7	70.4	70.2	73.2	70.0	0.3	4.0	0.6
8	81.2	83.5	82.3	81.3	2.8	1.4	0.1
9	85.6	84.8	85.4	85.3	0.9	0.2	0.4
10	74.8	72.9	77.0	75.5	2.5	2.9	0.9
11	70.2	70.9	69.9	70.3	1.0	0.4	0.1
12	88.2	87.8	90.2	87.5	0.5	2.3	0.8
mean ± SD	**80.3 ± 8.4**	**80.6 ± 9.0**	**80.7 ± 7.6**	**80.4 ± 8.6**	**1.6 ± 1.3**	**2.1 ± 1.2**	**0.6 ± 0.4**

Table 4. *Heart rate (HRV) values in milliseconds (ms) and % errors*

ID	Reference HRV	PPG Red HRV	PPG IR HRV	SCG HRV	PPG Red HRV % error	PPG IR HRV % error	SCG HRV % error
1	64.8	66.4	67.3	64.6	2.5	3.9	0.3
2	72.9	73.7	72.7	72.8	1.1	0.3	0.1
3	69.3	70.2	72.6	69.5	1.3	4.8	0.3
4	71.4	74.2	75.4	71.6	3.9	5.6	0.3
5	72.8	72.4	73.6	72.5	0.5	1.1	0.4
6	92.7	95.9	91.8	92.8	3.5	1.0	0.1
7	85.8	87.6	87.4	87.1	2.1	1.9	1.5
8	67.4	65.6	65.2	67.2	2.7	3.3	0.3
9	64.4	62.4	64.5	64.7	3.1	0.2	0.5
10	69.2	71.5	68.8	69.3	3.3	0.6	0.1
11	71.6	72.2	75.4	71.9	0.8	5.3	0.4
12	65.2	65.4	67.8	65.6	0.3	4.0	0.6
mean ± SD	**72.3 ± 8.6**	**73.1 ± 9.6**	**73.5 ± 8.4**	**72.5 ± 8.8**	**2.1 ± 1.2**	**2.6 ± 2.1**	**0.4 ± 0.5**

3.3. Respiration Rate and Temperature Computation Results

To extract respiratory rate (RR), two processing pipelines were employed, one based on dorso-ventral SCG and the other on PPG-Red. The % difference of the estimated respiration rates are provided in Table 5. For RR estimation, PPG-Red outperforms SCG with a significantly lower error rate (1.6 ± 1.5% vs. 3.9 ± 3.1%). While SCG is highly effective in capturing cardiac-induced vibrations, its sensitivity to respiratory patterns is relatively limited. SCG is acquired using an accelerometer placed on the chest, capturing mechanical vibrations resulting from both cardiac and respiratory activity. However, the respiratory component in SCG can be obscured by motion artifacts or inconsistencies in chest wall movement, which complicates reliable peak detection.

Finally, the temperature estimation yielded a mean percentage error of 3.7 ± 1.5%, indicating a reasonably accurate measurement, as shown in Table 5. This suggests that the thermal sensing approach used in the system is capable of capturing core temperature trends with acceptable precision for wearable applications. Minor deviations may stem from factors such as sensor placement, ambient temperature fluctuations, or motion-induced contact variability.

Table 5. *Respiration Rate (RR) values in breaths per minute (brpm), temperature values in ℃ and corresponding % errors*

ID	Reference Resp.	Reference Temp.	PPG Resp.	SCG Resp.	Temp.	PPG Resp. % error	SCG Resp. % error	Temp. % error
1	21.7	36.4	22.1	23.3	34.2	1.8	7.0	6.04
2	15.2	36.5	14.3	15.2	34.7	5.6	0.0	4.89
3	20.6	36.4	20.6	21.8	35.3	0.4	5.9	3.13
4	21.5	36.6	21.9	23.0	35.0	1.6	6.9	4.29
5	19.3	36.3	19.3	20.2	34.2	0.1	4.6	5.70
6	16.8	36.8	16.8	17.1	35.2	0.2	1.4	4.46
7	16.7	36.1	16.6	16.7	35.2	0.4	0.1	2.57
8	21.6	36.5	22.0	23.1	35.1	1.7	6.9	3.71
9	16.4	36.7	16.2	16.4	35.3	1.0	0.1	3.69
10	15.7	36.6	15.2	15.7	35.2	3.0	0.2	3.70
11	21.0	36.0	21.2	22.3	36.5	1.0	6.4	1.39
12	23.4	36.2	24.0	25.2	36.5	2.7	7.5	0.83
mean ± SD	**19.2±2.8**	**36.4±0.2**	**19.2±3.2**	**20.0±3.6**	**35.2±0.7**	**1.6±1.5**	**3.9±3.1**	**3.7±1.5**

3.4. Statistical Analyses

As seen in Table 6, for heart rate (HR), all modalities showed strong to excellent agreement with the reference, with Pearson's $r \geq 0.976$ and Spearman's $\rho \geq 0.925$ (both $p < 0.001$). SCG exhibited the narrowest LoA (-1.31 to 1.11 bpm) and lowest MAE (0.52 bpm), indicating the highest agreement among modalities, while PPG-IR showed the widest LoA. For heart rate variability (HRV), agreement was again highest for SCG ($r = 0.999$, ρ

= 0.993) with minimal bias (-0.175 ms) and very narrow LoA (-1.00 to 0.65 ms). PPG-red and PPG-IR maintained strong correlations but displayed wider LoA and higher errors. For respiration rate, SCG and PPG both had near-perfect correlations ($r \geq 0.998$, $\rho = 1.000$), though SCG demonstrated a significant bias (-0.842 brpm, $p = 0.002$) toward underestimation, while PPG showed no bias and very narrow LoA. For temperature, correlations with the reference were weak and not statistically significant ($r = -0.392$, $\rho = -0.196$), with a large positive bias (+1.225 °C) and wide LoA (-0.43 to 2.88 °C), indicating poor agreement. While this bias suggests limited accuracy, such deviations may still fall within tolerances acceptable for certain practical or clinical applications. Overall, SCG provided the most accurate HR and HRV measurements, PPG performed best for respiration without bias, and temperature estimation showed limited reliability.

3.5. Overall Discussion

It should be noted that the reported heart rate and respiration rate errors remained within the acceptable accuracy limits defined by the ISO 80601-2-61:2017 for heart rate and ISO 80601-2-55:2018 for respiration rate. On the other hand, temperature readings were not in alignment with the acceptable error ranges based on the ISO 80601-2-56:2017 (ISO, 2017a; 2017b; 2018).

The results demonstrate that SCG is the most reliable modality for HR and HRV estimation, likely due to its direct capture of cardiac mechanical activity with minimal susceptibility to optical artefacts. PPG-based methods, while slightly less accurate for HR and HRV, performed better for RR estimation, potentially because respiration-induced amplitude modulation is more pronounced in peripheral blood volume signals. The significant bias in SCG-derived RR may stem from sensitivity to motion artefacts and chest wall movement patterns. Temperature estimation showed poor agreement, which could be attributed to sensor placement, lack of calibration, and environmental temperature fluctuations; however, the observed bias may still be acceptable for non-critical monitoring where ±2 °C accuracy is sufficient. These findings highlight the importance of modality selection based on the target physiological parameter and suggest that further hardware and algorithmic refinements, particularly in temperature sensing and RR bias correction, could enhance overall system performance.

3.6. Limitations of the Study

Despite the promising performance of the proposed system, our study had some limitations. First, the study was conducted on a relatively small group of 12 healthy adult participants. While this was sufficient for preliminary validation, it may not fully capture the physiological variability found in broader populations such as pediatric or geriatric patients, individuals with chronic cardiopulmonary conditions, or those with abnormal rhythms or irregular breathing patterns. Second, data collection was performed in a controlled laboratory environment where participants remained stationary for five minutes. Although this allowed for clean signal acquisition and clear benchmarking against reference systems, it does not reflect the challenges of ambulatory monitoring. Lastly, while the system integrates a skin-contact temperature sensor that demonstrated acceptable

accuracy, it is important to note that skin temperature is inherently influenced by several external factors. Ambient temperature, local blood perfusion, sensor-skin contact pressure, and placement site variability can all affect the reliability of measurements. The limitation in temperature measurement accuracy suggests that the current implementation may not be suitable for applications requiring compliance with ISO 80601-2-56:2017 standards, and highlights the need for improved sensor calibration, placement optimization, and environmental compensation in future iterations of the system.

Table 6. *Agreement analysis between reference measurements and SCG-, PPG-, and temperature-based estimates for HR, HRV, respiration, and temperature*

Heart Rate						
Modality	**Pearson's r (p)**	**Spearman's ρ (p)**	**Bias (bpm)**	**95% LoA (bpm)**	**MAE (bpm)**	**Interpretation**
SCG	0.998 (<0.001)	0.991 (<0.001)	-0.10	-1.31 to 1.11	0.52	Excellent agreement, narrow LoA, no bias
PPG-red	0.984 (<0.001)	0.932 (<0.001)	-0.23	-3.48 to 3.03	1.28	Strong agreement, wider LoA, no bias
PPG-IR	0.976 (<0.001)	0.925 (<0.001)	-0.39	-4.21 to 3.42	1.68	Strong agreement, widest LoA, no bias
Heart Rate Variability						
Modality	**Pearson's r (p)**	**Spearman's ρ (p)**	**Bias (ms)**	**95% LoA (ms)**	**MAE (ms)**	**Interpretation**
SCG	0.999 (<0.001)	0.993 (<0.001)	-0.175	-1.00 to 0.65	0.31	Excellent agreement, narrow LoA, no bias
PPG-red	0.990 (<0.001)	0.930 (<0.001)	-0.833	-4.08 to 2.41	1.53	Strong agreement, wider LoA, no bias
PPG-IR	0.972 (<0.001)	0.914 (<0.001)	-1.250	-5.20 to 2.70	1.87	Strong agreement, widest LoA, no bias
Respiration						
Modality	**Pearson's r (p)**	**Spearman's ρ (p)**	**Bias (brpm)**	**95% LoA (brpm)**	**MAE (brpm)**	**Interpretation**
SCG	1.000 (<0.001)	1.000 (<0.001)	-0.842	-2.27 to 0.59	0.84	Perfect correlation, significant bias, narrow LoA
PPG	0.998 (<0.001)	1.000 (<0.001)	-0.025	-0.86 to 0.81	0.31	Excellent agreement, no bias, very narrow LoA
Temperature						
Modality	**Pearson's r (p)**	**Spearman's ρ (p)**	**Bias (°C)**	**95% LoA (°C)**	**MAE (°C)**	**Interpretation**
Temp.	-0.392 (0.208)	-0.196 (0.542)	1.225	-0.43 to 2.88	1.36	Weak/no correlation, large bias, wide LoA

Future work will focus on expanding the study to larger and more diverse populations, including dynamic, real-life conditions that better reflect everyday use. In parallel, improvements in temperature calibration and motion artifact resilience will be explored to enhance signal reliability across various environments and user profiles. In addition, integration of Bluetooth transmission and mobile interface capabilities can further enhance the system's applicability in telemedicine and remote patient monitoring scenarios.

4. CONCLUSION

This study introduces a miniaturized and multimodal wearable patch designed to monitor key cardiopulmonary parameters without the need for adhesive electrodes or bulky hardware. By integrating SCG, red/infrared PPG, and temperature sensing into a compact, low-power system, we achieved a balance between comfort, signal quality, and versatility. The proposed system effectively captured heart rate, heart rate variability and respiration rate using SCG and PPG modalities. The application of the Gaussian windowing and Teager-Kaiser Energy Operator significantly enhanced peak detection in the PPG and SCG signals, respectively, contributing to the system's robust cardiac signal extraction.

Overall, the results validate the feasibility and accuracy of the system for continuous, wearable cardiopulmonary assessment. Unlike many existing wearable systems that rely on adhesive electrodes or limited signal modalities, this device offers a truly electrode-free, miniaturized solution for multimodal cardiopulmonary monitoring.

CONFLICT OF INTEREST

The author declares no conflict of interest.

REFERENCES

Barnova, K., Martinek, R., Jaros, R., & Kahankova, R. (2020). Hybrid methods based on empirical mode decomposition for non-invasive fetal heart rate monitoring. *IEEE Access*, *8*, 51200-51218. https://doi.org/10.1109/ACCESS.2020.2980254

Carek, A. M., Conant, J., Joshi, A., Kang, H., & Inan, O. T. (2017). SeismoWatch: wearable cuffless blood pressure monitoring using pulse transit time. *Proceedings of the ACM on interactive, mobile, wearable and ubiquitous technologies*, *1*(3), 1-16. https://doi.org/10.1145/3130905

Centracchio, J., Parlato, S., Esposito, D., Bifulco, P., & Andreozzi, E. (2023). ECG-free heartbeat detection in seismocardiography signals via template matching. *Sensors*, *23*(10), 4684.

Chen, Y., Yang, X., Song, R., Liu, X., & Zhang, J. (2024). Predicting arterial stiffness from single-channel photoplethysmography signal: a feature interaction-based approach. *IEEE Journal of Biomedical and Health Informatics*, *28*(7), 3928-3941. https://doi.org/10.1109/JBHI.2024.3383234

cheol Jeong, I., Bychkov, D., & Searson, P. C. (2018). Wearable devices for precision medicine and health state monitoring. *IEEE Transactions on Biomedical Engineering*, *66*(5), 1242-1258. https://doi.org/10.1109/TBME.2018.2871638

Erin, E., & Semiz, B. (2023). *Spectral Analysis of Cardiogenic Vibrations to Distinguish Between Valvular Heart Diseases*. In: Proceedings of the 16th International Joint Conference on Biomedical Engineering Systems and Technologies (pp. 212-219). 16th International Conference on Bio-inspired Systems and Signal Processing, Lisbon, Portugal. https://doi.org/10.5220/0011663900003414

Etemadi, M., Inan, O. T., Heller, J. A., Hersek, S., Klein, L., & Roy, S. (2015). A wearable patch to enable long-term monitoring of environmental, activity and hemodynamics variables. *IEEE Transactions on Biomedical Circuits and Systems*, *10*(2), 280-288. https://doi.org/10.1109/TBCAS.2015.2405480

Fattah, S. A., Rahman, M. M., Mustakin, N., Islam, M. T., Khan, A. I., & Shahnaz, C. (2017, October 19-22). *Wrist-card: PPG sensor based wrist wearable unit for low cost personalized cardio healthcare system.* 2017 IEEE Global Humanitarian Technology Conference (GHTC), San Jose, CA, USA. https://doi.org/10.1109/GHTC.2017.8239326

Ganti, V. G., Carek, A. M., Nevius, B. N., Heller, J. A., Etemadi, M., & Inan, O. T. (2020). Wearable cuff-less blood pressure estimation at home via pulse transit time. *IEEE Journal of Biomedical and Health Informatics*, *25*(6), 1926-1937. https://doi.org/10.1109/JBHI.2020.3021532

Gupta, J. I., Shea, M. J., & Howlett, J. G. (2025). Cardiovascular Examination. MSD Manual. (Accessed:06/2025) https://www.msdmanuals.com/professional/cardiovascular-disorders/approach-to-the-cardiac-patient/cardiovascular-examination

Gupta, P., Moghimi, M. J., Jeong, Y., Gupta, D., Inan, O. T., & Ayazi, F. (2020). Precision wearable accelerometer contact microphones for longitudinal monitoring of mechano-acoustic cardiopulmonary signals. *NPJ Digital Medicine*, *3*(1), 19. https://doi.org/10.1038/s41746-020-0225-7

Hayirlioglu, Y. Z., & Semiz, B. (2024). PhysioPatch: A Multi-modal and Adaptable Wearable Patch for Cardiovascular and Cardiopulmonary Assessment. *IEEE Sensors Journal*, *24*(13), 21347-21357.https://doi.org/10.1109/JSEN.2024.3403846

Hurnanen, T., Lehtonen, E., Tadi, M. J., Kuusela, T., Kiviniemi, T., Saraste, A., Vasankari, T., Airaksinen, J., Koivisto, T., & Pänkäälä, M. (2016). Automated detection of atrial fibrillation based on time–frequency analysis of seismocardiograms. *IEEE Journal of Biomedical and Health Informatics*, *21*(5), 1233-1241. https://doi.org/10.1109/JBHI.2016.2621887

Inan, O. T., Baran Pouyan, M., Javaid, A. Q., Dowling, S., Etemadi, M., Dorier, A., Heller, J. A., Bicen, A. O., Roy, S., & De Marco, T. (2018). Novel wearable seismocardiography and machine learning algorithms can assess clinical status of heart failure patients. *Circulation: Heart Failure*, *11*(1), e004313. https://doi.org/10.1161/CIRCHEARTFAILURE.117.004313

Inan, O. T., Migeotte, P.-F., Park, K.-S., Etemadi, M., Tavakolian, K., Casanella, R., Zanetti, J., Tank, J., Funtova, I., & Prisk, G. K. (2014). Ballistocardiography and seismocardiography: A review of recent advances. *IEEE Journal of Biomedical and Health Informatics*, *19*(4), 1414-1427. https://doi.org/10.1109/JBHI.2014.2361732

ISO. (2017a). Medical electrical equipment — Part 2-56: Particular requirements for basic safety and essential performance of clinical thermometers for body temperature measurement (ISO 80601-2-56:2017). I. O. f. Standardization.

ISO. (2017b). Medical electrical equipment — Part 2-61: Particular requirements for basic safety and essential performance of pulse oximeter equipment (ISO 80601-2-61:2017). I. O. f. Standardization.

ISO. (2018). Medical electrical equipment — Part 2-55: Particular requirements for the basic safety and essential performance of respiratory rate monitoring equipment (ISO 80601-2-55:2018). I. O. f. Standardization.

Kaiser, J. F. (1990, April 03-06). *On a simple algorithm to calculate the'energy'of a signal*. In: International conference on acoustics, speech, and signal processing, Albuquerque, NM, USA. https://doi.org/10.1109/ICASSP.1990.115702

Klum, M., Urban, M., Tigges, T., Pielmus, A.-G., Feldheiser, A., Schmitt, T., & Orglmeister, R. (2020). Wearable cardiorespiratory monitoring employing a multimodal digital patch stethoscope: estimation of ECG, PEP, LVET and respiration using a 55 mm single-lead ECG and phonocardiogram. *Sensors*, *20*(7), 2033. https://doi.org/10.3390/s20072033

Lee, J., Matsumura, K., Yamakoshi, K.-i., Rolfe, P., Tanaka, S., & Yamakoshi, T. (2013). Comparison between red, green and blue light reflection photoplethysmography for heart rate monitoring during motion. 2013 35th annual international conference of the IEEE engineering in medicine and biology society (EMBC).

Li, S.-H., Lin, B.-S., Wang, C.-A., Yang, C.-T., & Lin, B.-S. (2017). Design of wearable and wireless multi-parameter monitoring system for evaluating cardiopulmonary function. *Medical Engineering & Physics*, *47*, 144-150. https://doi.org/10.1016/j.medengphy.2017.06.009

Lin, Y.-D., & Jhou, Y.-F. (2020). Estimation of heart rate and respiratory rate from the seismocardiogram under resting state. *Biomedical Signal Processing and Control*, *57*, 101779. https://doi.org/10.1016/j.bspc.2019.101779

Loro, F. L., Martins, R., Ferreira, J. B., de Araujo, C. L. P., Prade, L. R., Both, C. B., Nobre, J. C. N., Monteiro, M. B., & Dal Lago, P. (2024). Validation of a Wearable Sensor Prototype for Measuring Heart Rate to Prescribe Physical Activity: Cross-Sectional Exploratory Study. *JMIR Biomedical Engineering*, *9*, e57373. https://doi.org/10.2196/57373

Maeda, Y., Sekine, M., & Tamura, T. (2011). Relationship between measurement site and motion artifacts in wearable reflected photoplethysmography. *Journal of Medical Systems*, *35*, 969-976. https://doi.org/10.1007/s10916-010-9505-0

Nwibor, C., Haxha, S., Ali, M. M., Sakel, M., Haxha, A. R., Saunders, K., & Nabakooza, S. (2023). Remote health monitoring system for the estimation of blood pressure, heart rate, and blood oxygen saturation level. *IEEE Sensors Journal*, *23*(5), 5401-5411. https://doi.org/10.1109/JSEN.2023.3235977

Pandia, K., Inan, O. T., & Kovacs, G. T. (2013, July 03-07). *A frequency domain analysis of respiratory variations in the seismocardiogram signal*. In: 2013 35th Annual International Conference of the IEEE

Engineering in Medicine and Biology Society (EMBC), Osaka, Japan. https://doi.org/10.1109/EMBC.2013.6611139

Sana, F., Isselbacher, E. M., Singh, J. P., Heist, E. K., Pathik, B., & Armoundas, A. A. (2020). Wearable devices for ambulatory cardiac monitoring: JACC state-of-the-art review. *Journal of the American College of Cardiology*, *75*(13), 1582-1592. https://doi.org/10.1016/j.jacc.2020.01.046

Semiz, B. (2025). Clinical Validation of a Custom Wearable Patch for Accurate and Comfortable Vital Sign Monitoring in Pediatric Patients. *Acibadem Saglik Bilimleri Dergisi*, *16*(1). https://doi.org/10.31067/acusaglik.1569618

Semiz, B., Carek, A. M., Johnson, J. C., Ahmad, S., Heller, J. A., Vicente, F. G., Caron, S., Hogue, C. W., Etemadi, M., & Inan, O. T. (2020). Non-invasive wearable patch utilizing seismocardiography for peri-operative use in surgical patients. *IEEE Journal of Biomedical and Health Informatics*, *25*(5), 1572-1582. https://doi.org/10.1109/JBHI.2020.3032938

Shandhi, M. M. H., Semiz, B., Hersek, S., Goller, N., Ayazi, F., & Inan, O. T. (2019). Performance analysis of gyroscope and accelerometer sensors for seismocardiography-based wearable pre-ejection period estimation. *IEEE Journal of Biomedical and Health Informatics*, *23*(6), 2365-2374. https://doi.org/10.1109/JBHI.2019.2895775

Taebi, A., Solar, B. E., Bomar, A. J., Sandler, R. H., & Mansy, H. A. (2019). Recent advances in seismocardiography. *Vibration*, *2*(1), 64-86. https://doi.org/10.3390/vibration2010005

WHO. (2024). The top 10 causes of death. World Health Organization. (Accessed:06/2025) https://www.who.int/news-room/fact-sheets/detail/the-top-10-causes-of-death

Yang, C., Aranoff, N. D., Green, P., & Tavassolian, N. (2019). Classification of aortic stenosis using time–frequency features from chest cardio-mechanical signals. *IEEE Transactions on Biomedical Engineering*, *67*(6), 1672-1683. https://doi.org/10.1109/TBME.2019.2942741

Zavanelli, N., Kim, H., Kim, J., Herbert, R., Mahmood, M., Kim, Y.-S., Kwon, S., Bolus, N. B., Torstrick, F. B., & Lee, C. S. (2021). At-home wireless monitoring of acute hemodynamic disturbances to detect sleep apnea and sleep stages via a soft sternal patch. *Science Advances*, *7*(52), eabl4146.